https://doi.org/10.5194/egusphere-2026-3329
Preprint. Discussion started: 8 July 2026

Fibre-optic strain sensing on an alpine glacier

Robert Law[1, 2, 3, *], Mylène Jacquemart[1, 2, *], Matthias Bühler[4], Mauro A. Werder[1, 2], and Janosch Beer[1, 2]
[1]Laboratory of Hydraulics, Hydrology and Glaciology (VAW), ETH Zurich, Zurich, Switzerland
[2]Swiss Federal Institute for Forest, Snow and Landscape Research (WSL), bâtiment ALPOLE, Sion, Switzerland
[3]School of Geography and Planning, University of Sheffield, Sheffield, UK
[4]Marmota Engineering AG, Technopark Zurich, Zurich, Switzerland
[*]These authors contributed equally to this work.

Correspondence: Robert Law (robert.law@sheffield.ac.uk)

Abstract. In-situ measurements of ice deformation are constrained by the spatial resolution of discrete sensors, leaving fundamental questions about small-scale ice rheology unresolved. Here we present the first application of fibre-optic Distributed Strain Sensing (DSS) in a glacier setting, deployed at Chessjengletscher, a small polythermal glacier in the Swiss Alps. We compare Brillouin and Rayleigh DSS techniques in a borehole drilled to 38.4 m depth, alongside Raman distributed temperature sensing. Both methods resolve highly variable strain rates at the sub-metre scale — detail unattainable with conventional tiltmeters or inclinometry. Fitting observed strain profiles to a plane-strain deformation model supports a near-linear ice rheology for temperatures within 1 °C of the pressure melting point, consistent with recent laboratory experiments on temperate ice. Corresponding rate factors align closely with accepted values – though likely tempered by incomplete borehole freeze-in, which decouples the cable from ice deformation over portions of the column and introduces uncertainty into our displacement estimates. Brillouin offers a simpler field workflow and kilometre-scale measurement range compatible with remote deployment while Rayleigh provides superior spatial resolution but requires a demanding calibration procedure ill-suited to autonomous field use, though it shows promise for laboratory-scale deformation experiments. DSS represents a step change in englacial deformation measurement with direct implications for the study of ice rheology, glacier dynamics, and hazard assessment at alpine and ice-sheet scales.

1 Introduction

Glacier deformation studies are intrinsic to glaciology, yet in-situ observations of ice deformation are limited to discrete tiltmeters or inclinometry (a long history including Gerrard et al., 1952; Harper et al., 1998; Schwerzmann et al., 2006; Chandler et al., 2008; Lee et al., 2020; Roldán-Blasco et al., 2025) which have a low ceiling for spatial resolution due to device spacing and strain modulation through borehole casing, respectively, and which will miss rheological transitions unless one is fortunate with device placement (cf. Lüthi et al., 2003; Law et al., 2021). This contributes to an imperfect understanding of how ice rheology varies across small and large spatial scales – resulting from for example transitions between cold and temperate ice, variability in impurity content within ice layers, and fabric evolution – which in turn complicates our understanding of ice dynamics pertaining to glacier and ice-sheet motion, and to the stability and hazard assessment of glaciers. Laboratory experi-

https://doi.org/10.5194/egusphere-2026-3329
Preprint. Discussion started: 8 July 2026

ments (e.g. Glen, 1955; Mellor and Testa, 1969; Colbeck and Evans, 1973; Schohn et al., 2025) provide valuable information with regards to ice dynamics and material properties in (ideally) representative samples. But, in order to gain a more complete picture of how ice deformation can vary in natural settings, we need field-based high resolution measurements throughout the entire ice column.

In this regard, fibre-optic sensing presents a promising route forward. It offers sub-metre- to centimetre-scale spatial resolution for measuring a range of environmental variables with high accuracy by interrogating the wavelength or spectral properties of light backscattered along standard telecommunication fibre (in most use cases). This technology has been successfully deployed in glacier-settings for Distributed Acoustic Sensing (DAS; e.g. Booth et al., 2020; Fichtner et al., 2025; Gräff et al., 2025; see Table 1 for all acronyms) and distributed temperature sensing (DTS; e.g. Tyler et al., 2013; Law et al., 2021, 2024) revealing previously unexpected processes including localised brittle ice deformation, variable deformation rates within temperate ice, and calving-fjord-water interactions. However, despite steadily growing application in geotechnical (e.g. Marmota Engineering AG, 2012) and other environmental sensing (e.g. Schenato, 2017) settings, fibre-optic Distributed Strain Sensing (DSS) has not yet been used to measure ice deformation. If implemented successfully, DSS could provide high-resolution measurements of ice deformation that translate into a paradigm shift for understanding ice flow behaviour across alpine glacier and ice sheet settings.

Table 1. Fibre-optic acronyms reference

Acronym	Definition	Backscatter mode(s)
DAS	Distributed Acoustic Sensing	Rayleigh
DSS	Distributed Strain Sensing	Brillouin and Rayleigh
DTS	Distributed Temperature Sensing	Brillouin and Raman
OTDA	Optical Time-Domain Analysis	Brillouin
OTDR	Optical Time-Domain Reflectometry	Brillouin and Raman
C-OFDR	Coherent Optical Frequency-Domain Reflectometry	Rayleigh

To address this gap, we tested two DSS technologies, utilising Brillouin and Rayleigh backscatter (Fig. 2) deployed at Chessjengletscher, a small, polythermal glacier in Switzerland (Section 2.1, Fig. 1). Brillouin DSS exploits the frequency/wavelength dependency of Brillouin scattering on temperature and strain variations in the optical fibre (Culverhouse et al., 1989; Horiguchi et al., 1989; Tateda et al., 1990) when compared to a reference state. For Rayleigh DSS, on the other hand, the strained backscattered signal is cross-correlated with a reference backscatter profile (un-strained) to determine local spectral shifts induced by strain or temperature changes (Fig. 2C; Kreger et al., 2006). Here, we present results from an installation conducted in summer 2025, as well as a simple method for relating DSS measurements to parameters describing the flow of ice. Our findings reveal significant variation in ice deformation rates, and may indicate a near-linear rheology for ice within 1 °C of the pressure melting point.

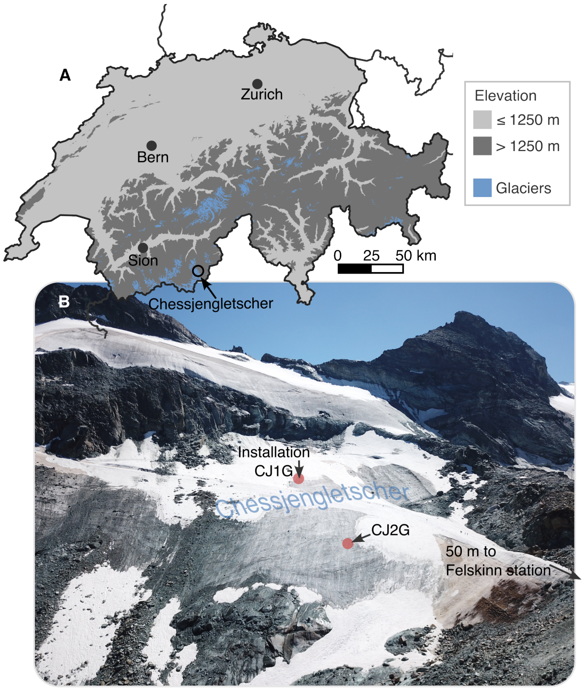

Figure 1. Chessjengletscher location within Switzerland. **A** Digital elevation model from Federal Office of Topography swisstopo (2005). Glacier polygons from Linsbauer et al. (2021). **B** Drone photo taken 7 August 2025. Fibre-optics were installed at CJ1G, with a further Geoprecision multi-sensor thermistor chain at CJ2G.

2 Methods

2.1 Study site

Chessjengletscher is a small (0.26 km^2), north-facing, two-part glacier located in Saastal, Canton of Vallais, ~50 m from the Felskinn gondola station within the Saas Fee ski resort (Fig. 1). This study focusses on the lower ice body (0.12 km^2) which extends from 2950-3080 m a.s.l. and has a clear polythermal structure, with a temperate core below the headwall, a cold terminus (though within 1-2 °C of zero degrees) and a basal temperate layer that progressively develops towards the terminus (present at CJ2G, Fig. A1; Beer et al., 2026). Historically, Chessjengletscher extended eastward across the Hinterer Allalinpass as part of a continuous glacier belt but in the extreme melt year of 2022 the final remnants of the eastern arm disappeared and the upper and lower sections of the glacier became separated by a steep headwall (Federal Office of Topography swisstopo, 2005). There are no detailed modelling studies of Chessjengletscher, but glaciers sharing this general geometry typically do not have complicated flow fields. Surface melt accounted for a surface lowering of around 2.5 m from installation on 7 August to our final measurement on 3 September 2025. Surface displacement at our installation site, CJ1G (Fig. 1) was 1.43 m a^{-1}, calculated on an annual basis (see Instrumentation).

2.2 Fibre optic sensing methodologies and background

Fibre-optic sensing exploits Raman, Brillouin, or Rayleigh back-scattering in optical fibres (though manufacturers actively try to minimize backscatter for information-transfer purposes), turning the entire cable into a continuous sensor that can be interrogated by pulses of light (Hartog, 2017). Rayleigh scattering is elastic, meaning the return photon energy matches the ingoing. Raman and Brillouin scattering, conversely, are inelastic processes. In these cases, energy is exchanged with discrete material vibrations: optical phonons (molecular vibrations) and acoustic phonons (lattice pressure waves) respectively.

Inelastic scattering produces four return signals (Fig. 2), two Stokes responses where the incident photon creates a phonon and loses energy (redshifting to a longer wavelength) and two anti-Stokes responses where the incident photon absorbs energy from an existing phonon (blueshifting to a shorter wavelength). One pair of Stokes, anti-Stokes signal is from Raman, one pair from Brillouin scattering. Raman sensing utilises the differential in temperature-dependent intensity of the Stokes and anti-Stokes signals while Brillouin sensing tracks shifts in frequency caused by acoustic phonons, which are sensitive to both temperature and mechanical strain. Rayleigh sensing typically exploits shifts in the spectral fingerprint of the return signal from an incident light swept over a limited wavelength range. There are numerous configurations and methods to utilise these backscatter signals in environmental fibre-optic sensing (Liu et al., 2025). Raman DTS can be used independently, while Brillouin and Rayleigh DSS require temperature information to correct for temperature-induced variations in the backscatter profile. Below we cover the methods used in this study in further detail.

Generally, two fibre setups are possible: single- and double-ended. In a single-ended setup only one end of the fibre is connected to the interrogator. In a double-ended setup both ends of the fibre are connected to the interrogator allowing backscatter to be measured in each direction which may help compensate for cable-damage artefacts, or to enable stimulated Brillouin sensing, where a pulse and a probe signal are launched from opposite ends to interact within the fibre (Thévenaz, 2010). In the event of cable failure, a double-ended methodology can revert to a single-ended alternative, though the abrupt fibre termination may result in a reflection spike that can saturate the interrogators detector.

2.2.1 Distributed strain sensing

In Brillouin DSS, changes in both temperature and strain along the fibre produce a frequency shift in the Brillouin Stokes and anti-Stokes components as a result of the inelastic scattering of acoustic phonons (Fig. 2; Horiguchi et al., 1995; Niklès, 1997; Soto et al., 2010). Brillouin measurements can be conducted with Optical Time-Domain Analysis (OTDA) or Optical Time-Domain Reflectometry (OTDR). Brillouin OTDA requires a double-ended setup, with a continuous probe laser firing down one end, coupled to a pulsed signal from the other end to utilise the stimulated version of Brillouin scattering (Thévenaz, 2010; Youn et al., 2024). The pulse signal interacts with the counter-propagating probe signal, which is swept across a range of frequencies to induce stimulated Brillouin scattering that reaches a peak intensity dependent on the temperature and strain state of the fibre. Conversely, OTDR launches a single laser pulse down one end of the fibre and tracks the frequency shift of the backscattered light as a function of travel time. Brillouin OTDA results in a much greater signal to noise ratio than Brillouin OTDR which has a weaker reflection signal but can be run as a single-ended setup. The range of our Omnisens

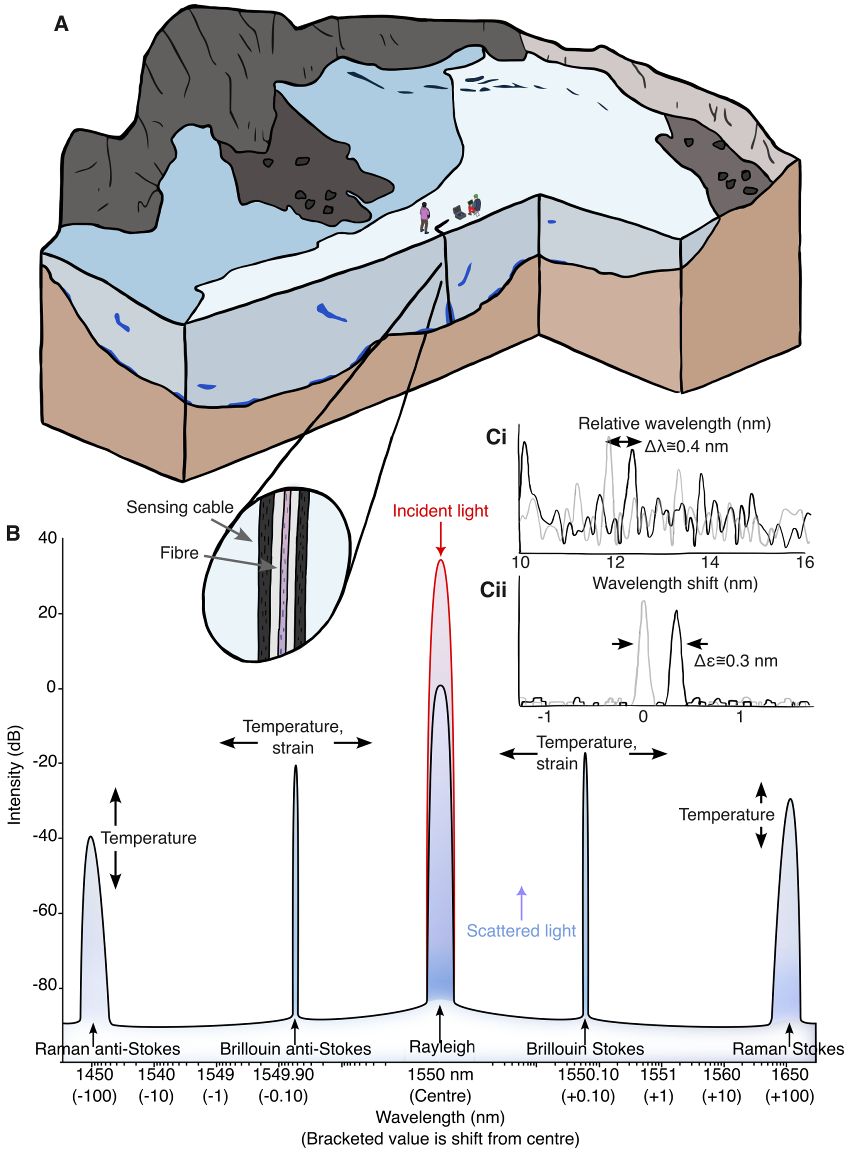

Figure 2. Fibre-optic installation, wavelengths, and C-OFDR methodology. **A** Sketch of borehole installation showing lack of refreezing or possible intersection with basal crevasse. The people are not to scale. **B** Rayleigh, Brillouin, and Raman values are representative and realistic, but not exact (Agrawal, 2013) and used to illustrate the orders of magnitude difference between incident light and backscatter wavelengths. **C** Adapted from Kreger et al. (2006) to illustrate how the relative wavelength is used to calculate a wavelength shift between a reference (black) and perturbed (grey) fibre as the input to Eq. 3. Note that the Rayleigh spectral shift in **C** represents the translation of the local interference pattern across the interrogator's swept-laser wavelength range, rather than an inelastic change in the scattered photon energy.

DT-208 interrogator is a 120 km loop, with no requirement that these follow the same path unlike with double-ended DTS (see Section 2.2.2). As a result of the temperature-dependence of Brillouin scattering, independent temperature measurements are required to decouple temperature and strain, with a thermo-optic effect of $\sim$44 $\mu\epsilon$ K^{-1} (micro-strain change per Kelvin). To derive the strain measurement, the technique utilizes the linear dependence of the Brillouin frequency shift, ν_B, on the applied longitudinal strain, δ, corrected for temperature, T.

The strain and temperature dependencies are governed by

$$\nu_B(\delta) = \nu_B(\delta_0)(1 + C_s\delta) \tag{1}$$

$$\nu_B(T) = \nu_B(T_r)[1 + C_T(T - T_r)] \tag{2}$$

where $\nu_B(\delta_0)$ and $\nu_B(T_r)$ are the Brillouin frequencies at a reference strain and temperature state, respectively, and C_s and C_T are the strain and temperature coefficients. For the silica fibres used in this study, these coefficients are approximately 4.6×10^{-5} and 9.5×10^{-5} K^{-1}, respectively (Horiguchi et al., 1995). By measuring this frequency shift and compensating for temperature effects, the specific strain distribution along the fibre can be resolved. We processed the data using the proprietary software provided by Omnisens (Omnisens Software Suite v400.4.7.0), though the underlying methodology following Eqs. 1 and 2 to solve for δ is straightforward. Brillouin systems generally offer a much higher return signal intensity than Rayleigh-based methods (Fig. 2), which facilitates greater accuracy within the same integration time. The Brillouin return signal becomes noisy for pulses shorter than 10 ns (distance along the fibre of 1 m) as this is comparable to the phonon lifetime in silica fibres (Horiguchi et al., 1995). Sampling can be finer than the 1 m resolution (0.25 m in our case) but this will reflect fibre conditions 0.5 m either side of the measurement point rather than strictly increasing the resolution.

We also performed high-resolution Rayleigh DSS measurements using Rayleigh backscatter Coherent Optical Frequency-Domain Reflectometry (C-OFDR), which offers cm-scale spatial resolution but which is both more methodologically complex and requires an interrogator that is much more delicate to handle. In practice, the effective resolution will also be modulated somewhat by the strength of the cable housing which transfers strain from the ice to the fibre. For our measurements, we used a Luna OBR 4600 Optical Backscatter Reflectometer, which utilises polarisation-diverse (light detected in two orthogonal states simultaneously) swept-wavelength interferometry to interrogate the fibre's Rayleigh backscatter as a function of length (Kreger et al., 2006). Unlike Brillouin scattering, where strain induces an inelastic change in the wavelength of the scattered light, Rayleigh-based C-OFDR quantifies strain by sweeping the incident light over a wavelength range to track the shift of the interference fingerprint created by microscopic impurities as the fibre physically elongates or changes temperature, effectively modelling the fibre as a weak fibre Bragg grating (Fig. 2C). (In standard usage, a fibre Bragg grating is a periodically-spaced modulation of the refractive index of the fibre that reflects only a specific narrow wavelength band, functioning as a wavelength-selective mirror, with the shift in the reflected wavelength used to provide information on fibre temperature and strain, Campanella et al., 2018.) The C-OFDR approach enables a spatial resolution far exceeding the 1 m limits of conventional OTDR and OTDA which would otherwise require picosecond-scale pulses to achieve comparable results. However, the range

https://doi.org/10.5194/egusphere-2026-3329
Preprint. Discussion started: 8 July 2026

of Rayleigh swept-wavelength interferometry is limited by laser coherence (though some methodologies exist to extend this; Ohno et al., 2016) which in our case means a range of 70 m with more accurate results (a 2 cm sampling window), or an extended range of up to 2 km with a reduced sampling resolution of 5 cm. These sampling windows are greater than the 1 cm maximum of our device, but it is useful to allow an overlap of gauges to improve the stability of the cross-correlation. Unlike for Brillouin OTDA, only a single-ended setup is necessary, but we utilised the full length of the installed looped fibre (and measured in both directions).

To derive strain, a cross-correlation is performed between the Rayleigh backscatter spectra obtained as a function of length through a Fourier transform (Soller et al., 2005) of a reference unperturbed state (after initial installation) and subsequent perturbed scans (follow-up measurements; Fig. 2C). Any local change in temperature or strain manifests as a spectral shift, $\Delta\lambda$, in the correlation peak given by

$$\frac{\Delta\lambda}{\lambda} = K_T \Delta T + K_\delta \delta \tag{3}$$

where K_T and K_δ are the temperature and strain coefficients, respectively, and λ is the backscatter wavelength with no disturbance. As with Brillouin DSS, proprietary software (LUNA Optical Backscatter Reflectometer v3.12.0) was required to processes the collected data, which was also corrected using independent temperature data for a temperature-strain cross-sensitivity in our setup of $\sim$31 $\mu\epsilon$ K^{-1}.

2.2.2 Distributed temperature sensing

Finally, we took DTS measurements using Raman backscatter and an APSensing DTS Linear Pro Series interrogator. Raman DTS operates by leveraging the dependence of the ratio between the anti-Stokes and Stokes components of Raman scattered return signals to fibre temperature (Fig. 2). A temperature time series at distance x along the cable comes from the standard Raman DTS equation

$$T(x) = \frac{\zeta}{ln\left(\frac{P_s(x)}{P_{a_s}(x)}\right) + C + \int_0^x \Delta\alpha(x')\,dx'} \tag{4}$$

where P_s and P_{a_s} are the Stokes and anti-Stokes power, ζ is a parameter dependent on fibre material which does not vary in time, and C is a dimensionless function of the alignment and sensitivity of the optical system, connectors, and splices that can vary with interrogator temperature and movement. The integral term is the integrated differential attenuation, where $\Delta\alpha(x')$ is equal to the attenuation of the Stokes wavelength minus the attenuation of the anti-Stokes wavelength and is non-zero as attenuation is related to wavelength. Differential attenuation can be caused by strain, sharp bends, and splices. In our case, a double-ended setup – where the DTS shoots laser pulses first in a forward direction and then in a reverse with the reasonable assumption that temperatures are equal in the forward and reverse directions – means that the integral term can be obtained independently. ζ and C are then obtained through separate calibration procedures. γ is calculated once through a controlled laboratory measurement at constant temperature while C is calculated at each time step using the lowermost thermistors in a thermistor chain that was installed alongside the fibre (see Instrumentation, below), with error-bound calculation and calibration handled by the open source Python 'dtscalibration' software package (des Tombe et al., 2020). See Law et al. (2021), which uses a near-identical setup, for further information.

2.3 Instrumentation

We drilled a borehole to the bed of Chessjengletscher (38.4 m) and subsequently instrumented it with two fibre-optic sensing cables (tight buffered for DSS, loose buffered for DTS) alongside discrete thermistors (Fig. 1). A tight-buffered cable has tight coupling between the cable housing and the fibre for optimum strain transfer, while a loose-buffered cable features around 1% overstuffing to minimise strain transfer. The tight-buffered cable featured a ribbed exterior for improved ice-cable coupling and housed one single-mode fibre while the loose-buffered cable contained one OM2+ multi-mode fibre and one G.657.A1 single-mode fibre. Both cables share a basal turnaround of diameter ~4.5 cm formed using a piece of scaffolding steel with a cylindrical steel weight attached to facilitate lowering down the water-filled borehole. Multi-mode fibres are preferred for Raman DTS as they result in greater scattering intensity, and the Raman signal is inherently weaker than the Brillouin signal (Fig. 2).

We used a GNSS (Global Navigation Satellite System) to record borehole positions and derive annual surface displacement rates (August 8, 2024–September 9, 2024) with an Emlid Reach GNSS processed through Emlid Flow with Real-time kinematic processing using Swiss Positioning Service. Both strain interrogators require ambient air temperatures above 10 °C to operate. We used a heated blanket and a well insulated sleeping bag and cover to facilitate this when air temperature fell below this value. We also measured the englacial temperature at CJ1G with a Geoprecision multi-sensor thermistor chain containing 10 TNodeHD nodes with a nominal accuracy of ±0.05°C, with sensors spaced 2.5 m apart from the glacier bed upward. A further Geoprecision chain with 5 thermistors was installed toward the glacier tongue (CJ2G, Fig. 1), with additional Tinytag chain installations covered in a concurrent study (Beer et al., 2026). All thermistors were calibrated to quantify sensor-specific offsets relative to 0°C in a temperature-controlled alcohol bath. Temperatures were logged at one-hour intervals, and mean temperatures derived from the time series, excluding the initial freeze-up phase of a few days, were used to construct a vertical temperature profile.

Following fibre installation on 7 August 2025 we took a reference measurement on 8 August and two follow-up measurements on 19 August and 3 September of the same year. The results presented here are between based on the two follow-up measurements, giving the cables a longer duration to freeze in. The Brillouin DSS measurements have a sampling resolution of 0.25 m and a 2 sigma strain repeatability of 10 $\mu\epsilon$. The Rayleigh DSS measurements have a sampling resolution of 2 cm (normal range) or 5 cm (extended range) and a strain resolution of 1 $\mu\epsilon$.

2.4 Calculating horizontal displacement from cable strain

To extract useful information regarding ice flow, we need to convert distributed strain to bed-parallel displacement. We follow a plane-strain approximation for ice deformation given the glacier's relatively simple geometry (and in keeping with most borehole inclinometry studies). This means we can relate along-cable strain to horizontal displacement under a simple Pythagorean

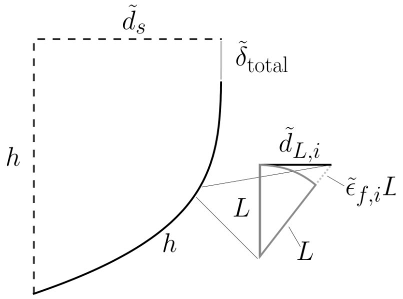

Figure 3. Schematic of profile fitting geometry using observation-constrained variables. See main text for symbol definitions. The displacement profile is for $n = 3$.

theorem approach. Measured displacement $\tilde{d}_{L,i}$ for each measurement interval L is given as

$$\tilde{d}_{L,i} = \sqrt{(L + \tilde{\epsilon}_{f,i}L)^2 - L^2} \tag{5}$$

where $\tilde{\epsilon}_{f,i}L$ is the recorded extension over the measurement period. L is a function of the interrogator and so is not influenced by ongoing cable deformation. Assuming constant deformation throughout the year, $\tilde{d}_{L,i}$ can then be multiplied by the measurement period, Δt, to obtain annual velocity in m a^{-1} (denoted $\tilde{u}_{L,i}$).

2.4.1 Fitting strain results for n and A

We can fit the observed cable strain profile to a theoretical displacement profile assuming a plane-strain approximation following Nye (1952) and Cuffey & Paterson (2010, Eq. 8.34). This horizontal displacement profile, $d(z)$, at a height z above the bed is given by

$$d(z) = d_{\text{s}} \left[1 - \left(1 - \frac{z}{h} \right)^{n+1} \right] \tag{6}$$

where d_{s} is the displacement due to internal ice deformation at the ice surface ($z = h$) over the measurement period, h is the total ice thickness, and n is the Glen's flow law exponent (see Fig. 3 for schematic illustration). Differentiating Eq. (6) with respect to depth gives the vertical gradient of horizontal displacement

$$\frac{\mathrm{d}d}{\mathrm{d}z} = d_{\text{s}} \frac{n+1}{h} \left(1 - \frac{z}{h} \right)^{n} . \tag{7}$$

To obtain d_s for each n we then use the bulk elongation of the cable as a physical constraint. The total integrated cable extension in the continuum case, δ_{total}, is defined by the difference between the arc length of the deformed cable and its vertical span

$$\delta_{\text{total}} = \int_0^h \sqrt{1 + \left(\frac{\mathrm{d}d}{\mathrm{d}z} \right)^2} \, \mathrm{d}z - h \, . \tag{8}$$

For any given test value of n, Eq. (8) is then solved numerically for the unique observation-constrained surface displacement $\tilde{d}_\text{s}$ that matches the calculated $\tilde{\delta}_\text{total}$ using a secant-method root-finding algorithm (`SciPy root_scalar`). This approach anchors the multiplication factor applied to the deformation profile (d_s) to observed total extension, meaning that the forward model for expected longitudinal cable strain, $\epsilon_f(z;n)$, becomes a function of the shape parameter n alone

$$\epsilon_f(z;n) = \sqrt{1 + \left(\frac{\mathrm{d}d(z;n)}{\mathrm{d}z}\right)^2} - 1\,. \tag{9}$$

Given observed cable strains $\tilde{\epsilon}_{f,i}$ at discrete heights z_i, the optimal n is found through a sweep from 0.5 to 4.0 by minimizing the root-mean-squared error (RMSE) cost function, $J(n)$

$$J(n) = \sqrt{\frac{1}{N}\sum_{i=1}^{N}\left[\tilde{\epsilon}_{f,i} - \epsilon_f(z_i;n)\right]^2}\,, \tag{10}$$

where N is the number of measurement intervals within our ice-column depth window.

Once the optimal exponent n is resolved from the geometric distribution of the strain, the corresponding Glen's flow law rate factor for the given n, A_eff, is calculated. The surface displacement over the measurement period is converted to an annual surface deformation velocity, $u_s = d_s/\Delta t$ and, following Cuffey & Paterson (2010, Eq. 8.35), A_eff is

$$A_\text{eff} = \frac{u_s(n+1)}{2(f\rho_i g\sin(\alpha)h)^n h} \tag{11}$$

where u_s is surface velocity due to ice deformation (excluding basal slip), ρ_i is the density of ice, g is acceleration due to gravity, α is surface slope, and h is ice thickness. f is a shape factor to account for the fact that the glacier is also supported by the valley walls and not an infinite slab (Cuffey & Paterson, 2010, Section 8.6.2.1), but we keep this as 1 given the relatively planar geometry of Chessjengletscher.

2.5 Rate factor A rescaled to $n = 3$

The A_eff obtained above is correct for a given n, but as A is most commonly stated for $n = 3$ it is useful to calculate A for the $n = 3$ case. working from the non-dimensional flow law derivation of Greve (2025) and setting a typical shear stress of

$$[\tau] = f\rho_i g\sin([\alpha])[h] \tag{12}$$

for typical slope and depth values, $[\alpha]$ and $[h]$ allows us to relate rate factors with different exponents. From $A_{n=3} = [\epsilon]\tilde{A}/[\tau]^3$ and $A_\text{eff} = [\epsilon]\tilde{A}/[\tau]^n$ where $A_{n=3}$ is the rate factor when $n = 3$, $\tilde{A}$ is the non-dimensional rate factor, and $[\epsilon]$ is the typical strain rate we can relate $A_{n=3}$ to A_eff as $A_{n=3} = A_\text{eff}/[\tau]^{3-n}$. Making the assumption that the typical $[h]$ and $[\alpha]$ for our setting are also valid locally (reasonable, given our drill-sites location in the middle of the glacier and a mean slope within 50 m of CJ1G is 20.2° compared to a slope of 21.6° across the lower Chessjen area as a whole as calculated with swissALTI3D elevation data; Federal Office of Topography swisstopo, 2024; Fig. 1) we obtain

$$A_{n=3} = \frac{u_s(n+1)}{2h}[\tau]^{-3}\,. \tag{13}$$

3 Results

Across all three measurement techniques we observed two sections of more uniform (relative to other parts of the profile, i.e. Fig. 4F) strain – between 23 m depth and the base, and between 14 m and 20 m depth (Fig. 4A). Strain within these sections still varies, with Rayleigh measurements exhibiting a notable periodic deformation pattern with amplitude $\sim$10 $\mu\epsilon$ and period $\sim$0.5 m, with shared characteristics between the two measurement ends (Fig. 4E). The level of detail in the Brillouin record is lower, but it also shows minor variations in these sections. Outside of these two regions strain is either positive and varying significantly (between 20 – 23 m depth; Fig. 4F), or slightly negative or neutral and still varying significantly (between 0 – 14 m depth) with the lower-sampling-resolution Brillouin record closely following the trend of the Rayleigh record, if not capturing the higher resolution features (Figs. 4A, E, F). All measurement records were in good agreement with one another throughout, with the exception of the Rayleigh extended record that departs from our other records outside of the more uniform strain sections, leading to a greater overall reported extension (Fig. 4B).

Both the cumulative strain profile (Fig. 4B) and annual displacement calculated through Pythagorean theorem under plane strain assumptions (Fig. 4C) broadly conform to the anticipated displacement pattern for linear or non-linear and shear-thinning rheology (Fig. 4C), with the small-scale strain variations much less discernable. The temperature had stabilised by the time we took the first follow-up measurement (Fig. A1), so we can exclude the scenario where negative strain rates are result of a temperature-change interference (Eqs. 2, 3). Our borehole location is temperate for the lowermost 5 m (Figs. 4D, A1), with a minimum temperature of $-1\,^{\circ}$C 5 m below the surface at the end of the measurement period. There is good agreement between DTS and thermistor records. The low level noise in the DTS record may be a result of the age of the interrogator (produced 2012 with no service history) though this has no bearing on the utility of the results. The annualised surface velocity exceeds the GNSS displacement by a factor of four – we explore possible reasons for this discrepancy in the Discussion.

The n fitting curves (Fig. 5B) are consistent across measurements with the Rayleigh technique in extended mode showing the greatest root-mean-squared error at every n value. Best fit values for n vary from 1.0 to 1.2, with smoothly increasing root-mean-squared error on both sides of the minima. The lower uniform strain section produces a notable misfit to the plane-strain profile profiles (Fig. 5A) for the best fit n of 1.2, while the remainder of the profile remains within a range of $\sim\pm$100 $\mu\epsilon$ (except for the Rayleigh measurements in extended mode). Values of A are dependent on n and surface slope (Fig. 6), but fall very close to the 'standard' A for $n = 3$ in Cuffey and Paterson (2010).

4 Discussion

Our continuous strain record demonstrates the efficacy and potential of DSS in glacier settings, revealing highly variable strain-rates and providing spatial resolutions far out of reach for discrete tiltmeter setups. This is already invaluable for alpine glaciers, but the continuous nature of DSS becomes even more attractive as the distance between sensors increases with increasing borehole depth (Doyle et al., 2018; Maier et al., 2019) making DSS highly promising for deep boreholes in ice-sheet settings. Our overall displacement profile largely conforms to plane-strain assumptions (Fig. 4C) but, within this broader picture, the

https://doi.org/10.5194/egusphere-2026-3329
Preprint. Discussion started: 8 July 2026

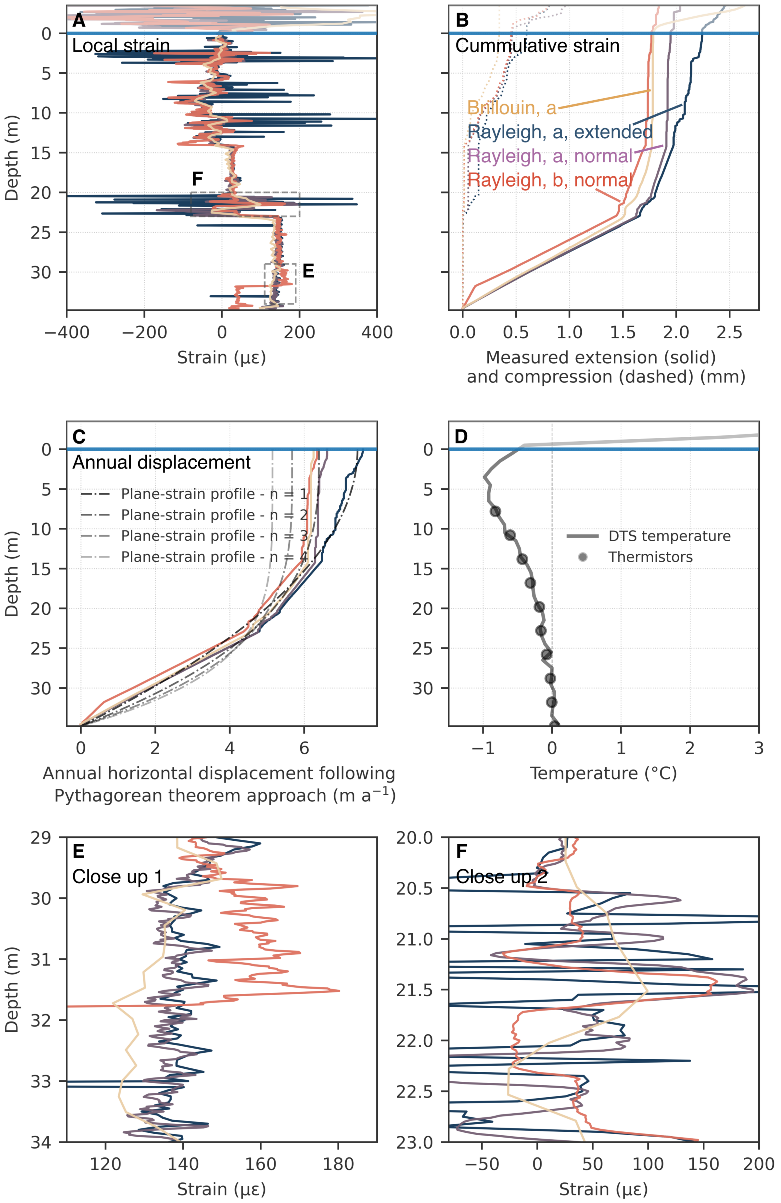

Figure 4. DSS and DTS results for the measurement interval 19 August – 3 September (annualised in panel C). See key in bottom right for fibre colours. ‘a’ and ‘b’ refer to the two different sides of the looped fibre. Blue horizontal line at depth 0 m is the ice surface position on 3 September. **A** Strain along the fibre. **B** Cumulative positive and negative strain along the fibre. **C** Horizontal displacement calculated through a Pythagorean theorem approach (Eq. 5; coloured lines) and theoretical overall profiles (Eq. 6) faithful to total fibre extension in grey-scale dot dash, both assuming plane-strain deformation. **D** DTS temperature record and thermistor measurements. **E** and **F** Close ups from **A**.

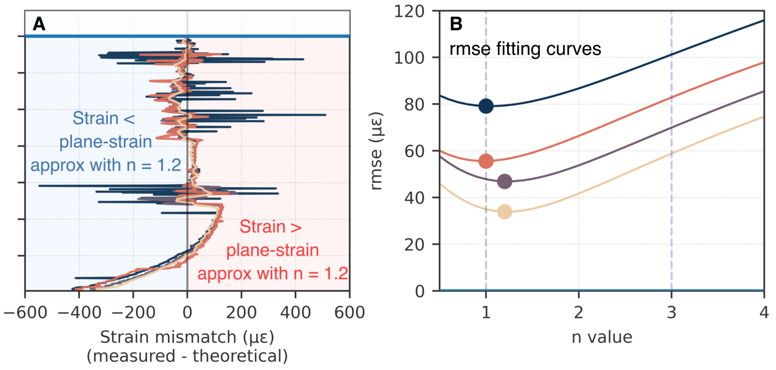

Figure 5. Fitting theoretical strain to measured strain Colour coding as in Fig. 4. **A** mismatch between a plane-strain profile with $n = 1.2$ and each measurement record. **B** root-mean-squared error for each measurement record with varying n

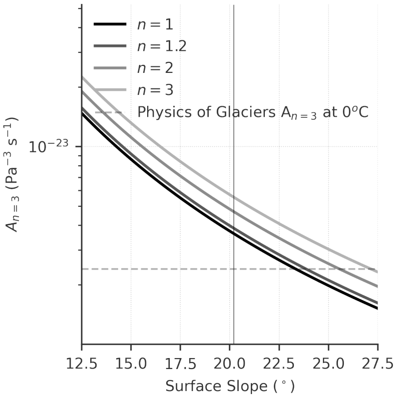

Figure 6. $A_{n=3}$ **for our study site calculated with varying surface slope and** n. Dashed horizontal line shows the 'standard' A for $n = 3$ for temperate ice in Cuffey and Paterson (2010). The thin vertical line traces the 20.2° slope calculated within a 50 m radius of site CJ1G.

section where we can be confident of full freeze in (20 – 23 m; Fig. 4F) exhibits highly variable strain rates indicative of an ice rheology that varies substantially with grain size or impurity content (Cuffey et al., 2000).

The detail in the firmly frozen sections demonstrates that DSS, and Rayleigh DSS in particular, can record ice deformation at incredibly high resolution. However, DSS is not immune to the problem of slowly-refreezing boreholes in temperate ice, or to the assumption of plane strain carried in most borehole strain surveys. Temperate-ice boreholes will refreeze, but only at a rate of ∼1 mm per week (Harrison, 1972), with the time to full freeze lengthened significantly if a (basal) crevasse (Walter et al., 2010) or englacial channel was intersected. In our installation, a lack of freeze-in may explain the vertically continuous uniform strain sections (Fig. 4A) which would necessitate highly unusual rheological properties or stress conditions if the cable was fully coupled. This may indicate that the cable is pinned at the bottom of the borehole (either at the borehole end point strictly, or dragged some distance due to sliding) resulting in near-uniform strain values over this depth range (shown

https://doi.org/10.5194/egusphere-2026-3329
Preprint. Discussion started: 8 July 2026

schematically in Fig. 2). Relatedly, our Pythagorean theorem approach to calculating displacement will be unrepresentative if basal slip is translated up through the column due to a lack of freeze in: a basal slip displacement of 1 cm would correspond to 1 cm of surface displacement, but contribute in our calculation with Eq. 5 to a displacement of 44 cm if distributed evenly through plane strain over a 10 m length.

There are several reasons for why we might be getting a mismatch between the strain-derived total displacements and the GNSS-derived displacement. For one, basal slip entering into the lower near-uniform strain section may explain the larger calculated surface displacement (6 m a^{-1}) against the GNSS recording of 1.43 m a^{-1}, though we note that annual displacement from 23 m depth upwards still matches total surface displacement. Alternatively, or in addition, the glacier could be moving faster than average over the two week measurement period. Seasonal basal freezing may be present in parts of the glacier tongue (Beer et al., 2026), but while this will have a large influence on basal slip, we would not expect a large influence on internal deformation (though not absent; Maier et al., 2022). Further, while we have high confidence that the strain profile is correct, especially given the close agreement between methodologies, it could be that our Pythagorean theorem approach converts non-plane-strain dynamics into plane strain. Having two axes for tilt-measurements can help reduce and quantify this problem (Harper et al., 2001; Keller and Blatter, 2012; Maier et al., 2022), but is unavailable in fibre-optic DSS setups. Alternatively, our record could be capturing ‘glacier settling’ processes due to the insertion of the borehole but we view the latter possibility as less feasible given that the shape of the profile, with increasing deformation at depth, is broadly in agreement with theoretical expectations (Fig. 4C).

For most glacier modelling applications and for both alpine glacier and ice-sheet settings, n=3 remains the most commonly utilised exponent value in Glen’s Flow Law. For temperate glaciers, or those close to the pressure-and-solute-dependent melting point (Lliboutry, 1996), however, recent laboratory experiments (Adams et al., 2021; Schohn et al., 2025) and less recent borehole tiltmeter experiments (Gerrard et al., 1952) suggest a value of n at or slightly above 1. While, for cold polar ice sheets $n = 4$ is suggested (Bons et al., 2018; Millstein et al., 2022; Ranganathan and Minchew, 2024). This is important not just for internal ice rheology, but also basal sliding, as the value of n exerts a strong control on the basal stress state and the ability of ice to creep around basal obstacles, with temperate ice found at the base of otherwise cold glacier systems (e.g. Law et al., 2021, 2023). Our results align well with an n near one, providing support for the use and exploration of this value in numerical models for (near-)temperate ice. However, full freeze in at the base would significantly increase our confidence in our determination of n. Further, our calculations for A are well-matched with reference values from Cuffey and Paterson (2010) for temperate ice (an A of 2.37×10^{-24} Pa^{-3} s^{-1}), with a best fit n of 1.2 producing an $A_{n=3}$ of 3.83×10^{-24} Pa^{-3} s^{-1}. If our DSS-derived displacement was lower, and therefore in line with with surface displacement, our $A_{n=3}$ value would be lower than most reported values. A full 3D model (Harper et al., 1998; Roldán-Blasco et al., 2025) and a larger borehole array would facilitate greater certainty in our calculated displacement, n, and A values but our location provides a surprisingly robust ‘field laboratory’ where new technologies can be tested yet still provide rheologically useful information.

In light of the above, and considerations about deployability, we make several recommendations for future studies. Whereas a tiltmeter placed at the ice-bed interface will be evident through it settling in a horizontal orientation, the possible ambiguity in a DSS setup if the borehole has not frozen makes it advisable to keep the fibre termination or turnaround slightly above the ice-bed interface. We drilled our borehole relatively late in the melt season, but would suggest that drilling early in the melt season would provide a better time-frame to allow the cable to freeze in as fully as possible. Repeat measurements can then be taken at a greater interval before the onset of winter precludes access and interrogator operation. Alternatively, repeat measurements may be taken in the following melt season. However, with a maximum cable extension limit of 1% this will increase the risk of cable failure prior to measurement (though cables often function somewhat past manufacturer specifications, Law et al., 2021). While we used a ribbed cable design, the development of purpose-built ice-grip points (for example evenly spaced metal disks) may also help alleviate the issue of ice-cable coupling in temperate ice. Full borehole freeze is not a problem for cold-ice settings (Law et al., 2021), but it would be important to ensure liquid water is present to allow freeze-in in otherwise dry boreholes drilled through mechanical action.

Unlike with widely available DTS interrogators, neither DSS device is suitable for autonomous deployment in a glacier setting in it's 'off-the-shelf' state. However, the long measurement range of the Omnisens Brillouin interrogator means that it could be set up in a protected and powered environment many kilometres from the field site. For Rayleigh DSS, a time consuming (∼20 min) and delicate device calibration procedure is required before each measurement, which must be repeated following even small movements or changes of ambient temperatures of the device. As a result, of the techniques tested here, we found the Brillouin OTDA approach more suitable for field deployments on glaciers. That said, Rayleigh DSS offers exciting opportunities for high resolution measurements, both in the field or in lab-based sheer ring experiments of ice and sediment deformation where existing methodology usually depends on visual monitoring of bead chains (Zoet and Iverson, 2020), tracers (Adams et al., 2021), tiltmeters (Schohn et al., 2025), or plate movement (Wilson and Peternell, 2012; Qi et al., 2019).

Overall, our results demonstrate the efficacy of DSS in revealing sub-metre deformation throughout the ice column and its potential in advancing our understanding of ice rheology and dynamics across glacier and ice sheet settings. In alpine glaciers and ice sheets alike, DSS could yield valuable insights into the transition between cold and temperate ice, and how this affects sliding and stress transfer. This is directly relevant, for example, for understanding and predicting how basal warming may affect the stability of cold hanging glaciers (e.g., Vincent et al., 2015; Troilo et al., 2021, 2022). DSS is equally promising for scientific investigations of ice sheets. Here, DSS may be able to isolate the exact rheological influence of the transition from interglacial- to glacial-phase ice (Lüthi et al., 2003; Law et al., 2021)), the role of dirty basal (Hubbard and Sharp, 1995) or temperate (Krabbendam, 2016; Law et al., 2021) ice, and even the transition from ice to sediment deformation in Antarctic ice streams (Alley et al., 1986). Beyond glaciology, high-precision borehole DSS could also serve to investigate the connections between permafrost temperature changes and deep-seated instabilities (e.g. Patton et al., 2019; Hjort et al., 2022; Kääb et al., 2018). Together, the capabilities of DSS position it as a transformative tool in cryospheric research that can constrain long-standing uncertainties in ice rheology from grain-scale to ice-sheet scales.

Code and data availability. Processing scripts and datasets used to generate Fig. 4 can be found here. This repository will be finalised following peer review.

https://doi.org/10.5194/egusphere-2026-3329
Preprint. Discussion started: 8 July 2026

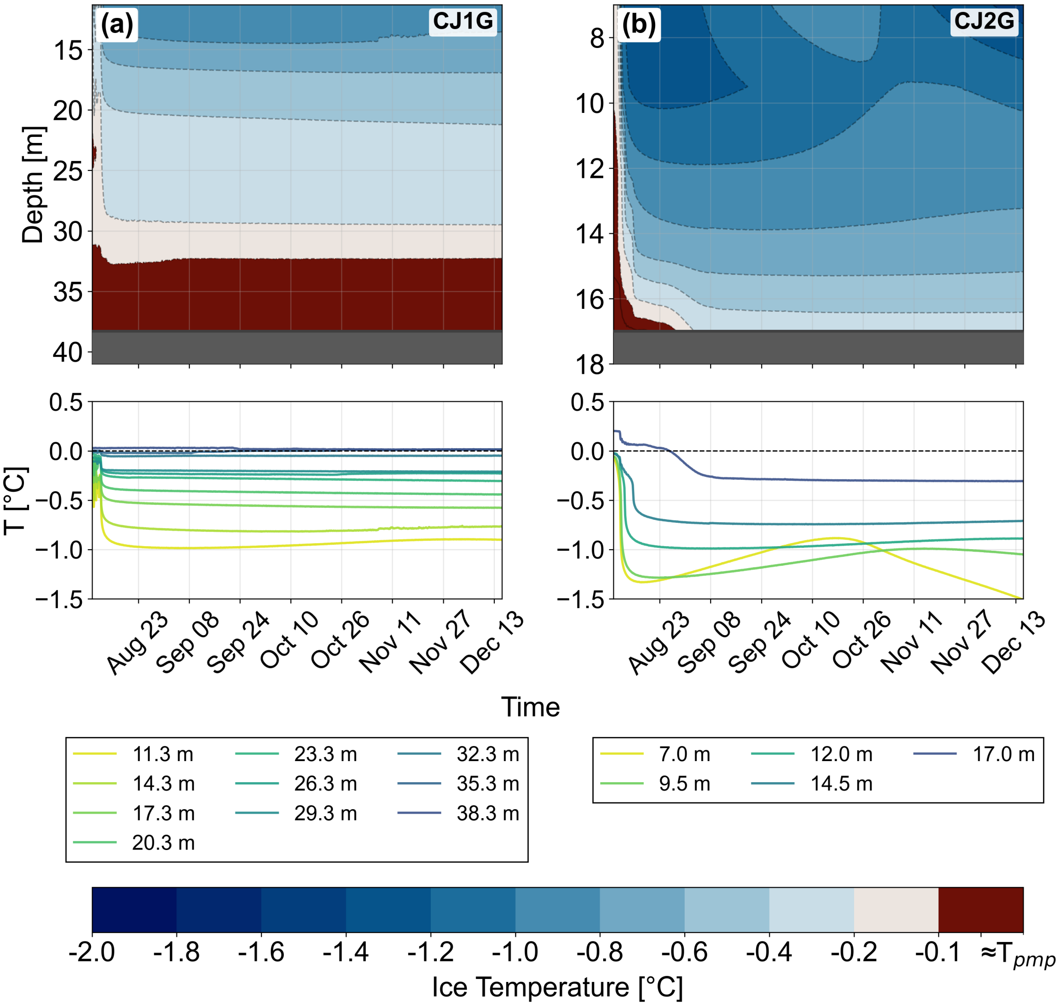

Figure A1. Thermistor time profiles for sites CJ1G and CJ2G for dates in 2025. Coloured lines correspond to thermistor installation depths.

Author contributions. MJ, RL, and MW wrote the FIBR-ICE Swiss Polar Institute Techno-grant proposal and the POLYDEF WSL proposal. MJ, RL, MB, and JB participated in fieldwork. MB processed the DSS data and provided technical guidance on DSS. RL processed the DTS data. JB processed the thermistor and GNSS data. MW assisted in the analytical components of the paper. RL wrote the manuscript and produced the figures with input from all co-authors.

Competing interests. MB is employed by Marmota Engineering AG who were contracted by ETH Zurich to deploy and process strain data. There are no other conflicts of interest to declare for this manuscript.

Acknowledgements. This project was partially funded through a Swiss Polar Institute Techno-grant (FIBR-ICE) and through a Swiss Federal Institute for Forest, Snow and Landscape Research internal grant (POLYDEF). RL was funded by an ETH Fellows grant, a Leverhulme Trust Early Career Fellowship (Unifying ice-sheet sliding relationships to improve sea level rise predictions), and the University of Sheffield. Large language models (Google Gemini) were used to scan literature, assess and improve readability and flow of selected passages, and implement and improve code incrementally. Any and all alterations were thoroughly checked by hand'.

References

Adams, C. J., Iverson, N. R., Helanow, C., Zoet, L. K., and Bate, C. E.: Softening of Temperate Ice by Interstitial Water, Frontiers in Earth Science, 9, 702 761, https://doi.org/10.3389/feart.2021.702761, 2021.

Agrawal, G.: Nonlinear Fiber Optics, Elsevier, 5 edn., https://doi.org/10.1016/C2011-0-00045-5, 2013.

Alley, R. B., Blankenship, D. D., Bentley, C. R., and Rooney, S. T.: Deformation of till beneath ice stream B, West Antarctica, Nature, 322, 57–59, https://doi.org/10.1038/322057a0, 1986.

Beer, J., Jacquemart, M., Huss, M., Santin, I., Clara Racz, G., Ogier, C., Gindraux, S., Hösli, L., Moser, R., Irving, J., Fischer, M., and Farinotti, D.: Polythermal conditions in small glaciers in the Swiss Alps, https://doi.org/10.5194/egusphere-2026-3042, 2026.

Bons, P. D., Kleiner, T., Llorens, M.-G., Prior, D. J., Sachau, T., Weikusat, I., and Jansen, D.: Greenland Ice Sheet: Higher Nonlinearity of Ice Flow Significantly Reduces Estimated Basal Motion, Geophysical Research Letters, 45, 6542–6548, https://doi.org/10.1029/2018GL078356, 2018.

Booth, A. D., Christoffersen, P., Schoonman, C., Clarke, A., Hubbard, B., Law, R., Doyle, S. H., Chudley, T. R., and Chalari, A.: Distributed Acoustic Sensing of Seismic Properties in a Borehole Drilled on a Fast-Flowing Greenlandic Outlet Glacier, Geophysical Research Letters, 47, https://doi.org/10.1029/2020GL088148, 2020.

Campanella, C., Cuccovillo, A., Campanella, C., Yurt, A., Passaro, V., Campanella, C. E., Cuccovillo, A., Campanella, C., Yurt, A., and Passaro, V. M. N.: Fibre Bragg Grating Based Strain Sensors: Review of Technology and Applications, Sensors, 18, 3115, https://doi.org/10.3390/s18093115, 2018.

Chandler, D., Hubbard, B., Hubbard, A., Murray, T., and Rippin, D.: Optimising ice flow law parameters using borehole deformation measurements and numerical modelling, Geophysical Research Letters, 35, L12 502, https://doi.org/10.1029/2008GL033801, 2008.

Colbeck, S. C. and Evans, R. J.: A Flow Law for Temperate Glacier Ice, Journal of Glaciology, 12, 71–86, https://doi.org/10.3189/s0022143000022711, 1973.

Cuffey, K. M. and Paterson, W. S. B.: The Physics of Glaciers, Elsevier Science & Technology Books, Amsterdam, 4 edn., 2010.

Cuffey, K. M., Conway, H., Gades, A., Hallet, B., Raymond, C. F., and Whitlow, S.: Deformation properties of subfreezing glacier ice: Role of crystal size, chemical impurities, and rock particles inferred from in situ measurements, Journal of Geophysical Research: Solid Earth, 105, 27 895–27 915, https://doi.org/10.1029/2000JB900271, 2000.

Culverhouse, D., Farahi, F., Pannell, C., and Jackson, D.: Potential of stimulated Brillouin scattering as sensing mechanism for distributed temperature sensors, Electronics Letters, 25, 913–915, https://doi.org/10.1049/el:19890612, 1989.

des Tombe, B., Schilperoort, B., and Bakker, M.: Estimation of Temperature and Associated Uncertainty from Fiber-Optic Raman-Spectrum Distributed Temperature Sensing, Sensors, 20, 2235, https://doi.org/10.3390/s20082235, 2020.

Doyle, S. H., Hubbard, B., Christoffersen, P., Young, T. J., Hofstede, C., Bougamont, M., Box, J. E., and Hubbard, A.: Physical Conditions of Fast Glacier Flow: 1. Measurements From Boreholes Drilled to the Bed of Store Glacier, West Greenland, Journal of Geophysical Research: Earth Surface, 123, 324–348, https://doi.org/10.1002/2017JF004529, 2018.

Federal Office of Topography swisstopo: DHM25 – Digital Height Model of Switzerland, https://www.swisstopo.admin.ch/en/height-model-dhm25, 2005.

Federal Office of Topography swisstopo: swissALTI3D – Digital Elevation Model of Switzerland and the Principality of Liechtenstein, https://www.swisstopo.admin.ch/en/height-model-swissalti3d, 2024.

Fichtner, A., Hofstede, C., Kennett, B. L. N., Svensson, A., Westhoff, J., Walter, F., Ampuero, J.-P., Cook, E., Zigone, D., Jansen, D., and Eisen, O.: Hidden cascades of seismic ice stream deformation, Science, 387, 858–864, https://doi.org/10.1126/science.adp8094, 2025.

Gerrard, J. A. F., Perutz, M. F., Roch, A., and Taylor, G. I.: Measurement of the velocity distribution along a vertical line through a glacier, Proceedings of the Royal Society of London. Series A. Mathematical and Physical Sciences, 213, 546–558, https://doi.org/10.1098/RSPA.1952.0144, 1952.

Glen, J. W.: The creep of polycrystalline ice, Proceedings of the Royal Society of London. Series A. Mathematical and Physical Sciences, 228, 519–538, https://doi.org/10.1098/rspa.1955.0066, 1955.

Gräff, D., Lipovsky, B. P., Vieli, A., Dachauer, A., Jackson, R., Farinotti, D., Schmale, J., Ampuero, J.-P., Berg, E., Dannowski, A., Kneib-Walter, A., Köpfli, M., Kopp, H., van der Loo, E., Mata Flores, D., Mercerat, D., Moser, R., Sladen, A., Walter, F., Wasser, D., Welty, E., Wetter, S., and Williams, E. F.: Calving-driven fjord dynamics resolved by seafloor fibre sensing, Nature, 644, 404–412, https://doi.org/10.1038/s41586-025-09347-7, 2025.

Greve, R.: On non-dimensional forms of basal sliding laws and flow laws for ice-sheet and glacier modelling, Journal of Glaciology, 71, e123, https://doi.org/10.1017/jog.2025.10100, 2025.

Harper, J. T., Humphrey, N. F., and Pfeffer, W. T.: Three-Dimensional Deformation Measured in an Alaskan Glacier, Science, 281, 1340–1342, https://doi.org/10.1126/science.281.5381.1340, 1998.

Harper, J. T., Humphrey, N. F., Pfeffer, W. T., Huzurbazar, S. V., Bahr, D. B., and Welch, B. C.: Spatial variability in the flow of a valley glacier: Deformation of a large array of boreholes, Journal of Geophysical Research: Solid Earth, 106, 8547–8562, https://doi.org/10.1029/2000JB900440, 2001.

Harrison, W. D.: Temperature of a Temperate Glacier, Journal of Glaciology, 11, 15–29, https://doi.org/10.3189/S0022143000022450, 1972.

Hartog, A. H.: An Introduction to Distributed Optical Fibre Sensors, CRC Press, https://doi.org/10.1201/9781315119014, 2017.

Hjort, J., Streletskiy, D., Doré, G., Wu, Q., Bjella, K., and Luoto, M.: Impacts of permafrost degradation on infrastructure, Nature Reviews Earth & Environment, 3, 24–38, https://doi.org/10.1038/s43017-021-00247-8, 2022.

Horiguchi, T., Kurashima, T., and Tateda, M.: Tensile strain dependence of Brillouin frequency shift in silica optical fibers, IEEE Photonics Technology Letters, 1, 107–108, https://doi.org/10.1109/68.34756, 1989.

Horiguchi, T., Shimizu, K., Kurashima, T., Tateda, M., and Koyamada, Y.: Development of a distributed sensing technique using Brillouin scattering, Journal of Lightwave Technology, 13, 1296–1302, https://doi.org/10.1109/50.400684, 1995.

Hubbard, B. and Sharp, M.: Basal ice facies and their formation in the Western Alps, Arctic & Alpine Research, 27, 301–310, https://doi.org/10.2307/1552023, 1995.

Kääb, A., Leinss, S., Gilbert, A., Bühler, Y., Gascoin, S., Evans, S. G., Bartelt, P., Berthier, E., Brun, F., Chao, W.-A., Farinotti, D., Gimbert, F., Guo, W., Huggel, C., Kargel, J. S., Leonard, G. J., Tian, L., Treichler, D., and Yao, T.: Massive collapse of two glaciers in western Tibet in 2016 after surge-like instability, Nature Geoscience, 11, 114–120, https://doi.org/10.1038/s41561-017-0039-7, 2018.

Keller, A. and Blatter, H.: Measurement of strain-rate components in a glacier with embedded inclinometers, Journal of Glaciology, 58, 692–698, https://doi.org/10.3189/2012JoG11J234, 2012.

Krabbendam, M.: Sliding of temperate basal ice on a rough, hard bed: creep mechanisms, pressure melting, and implications for ice streaming, The Cryosphere, 10, 1915–1932, https://doi.org/10.5194/tc-10-1915-2016, 2016.

Kreger, S. T., Gifford, D. K., Froggatt, M. E., Soller, B. J., and Wolfe, M. S.: High Resolution Distributed Strain or Temperature Measurements in Single- and Multi-mode Fiber Using Swept-Wavelength Interferometry, OSA Technical Digest (CD), p. ThE42, 2006.

Law, R., Christoffersen, P., Hubbard, B., Doyle, S. H., Chudley, T. R., Schoonman, C., Bougamont, M., des Tombe, B., Schilperoort, B., Kechavarzi, C., Booth, A., and Young, T. J.: Thermodynamics of a fast-moving Greenlandic outlet glacier revealed by fiber-optic distributed temperature sensing, Science Advances, 7, eabe7136, https://doi.org/10.1126/sciadv.abe7136, 2021.

Law, R., Christoffersen, P., MacKie, E., Cook, S., Haseloff, M., and Gagliardini, O.: Complex motion of Greenland Ice Sheet outlet glaciers with basal temperate ice, Science Advances, 9, eabq5180, https://doi.org/10.1126/sciadv.abq5180, 2023.

Law, R., Gimbert, F., Christoffersen, P., Vincent, C., and Piard, L.: High-Altitude Glacier Warming Mechanisms and Dynamics Revealed Through Fibre-Optic Sensing, in: AGU Fall Meeting Abstracts, p. C31B06, American Geophysical Union, Washington D.C., 2024.

Lee, I. R., Hawley, R. L., Bernsen, S., Campbell, S. W., Clemens-Sewall, D., Gerbi, C. C., and Hruby, K.: A novel tilt sensor for studying ice deformation: application to streaming ice on Jarvis Glacier, Alaska, Journal of Glaciology, 66, 74–82, https://doi.org/10.1017/jog.2019.84, 2020.

Linsbauer, A., Huss, M., Hodel, E., Bauder, A., Fischer, M., Weidmann, Y., Bärtschi, H., and Schmassmann, E.: The New Swiss Glacier Inventory SGI2016: From a Topographical to a Glaciological Dataset, Frontiers in Earth Science, 9, https://doi.org/10.3389/feart.2021.704189, 2021.

Liu, L., Duda, M. I., Salazar Vásquez, A. F., and Berntsen, A. N.: A review of fiber optic sensing in geomechanical applications at laboratory and field scales, Geomechanics for Energy and the Environment, 43, 100 699, https://doi.org/10.1016/j.gete.2025.100699, 2025.

Lliboutry, L.: Temperate ice permeability, stability of water veins and percolation of internal meltwater, Journal of Glaciology, 42, 201–211, https://doi.org/10.3189/s0022143000004068, 1996.

Lüthi, M. P., Funk, M., and Iken, A.: Indication of active overthrust faulting along the Holocene-Wisconsin transition in the marginal zone of Jakobshavn Isbræ, Journal of Geophysical Research, 108, 2543, https://doi.org/10.1029/2003JB002505, 2003.

Maier, N., Humphrey, N., Harper, J., and Meierbachtol, T.: Sliding dominates slow-flowing margin regions, Greenland Ice Sheet, Science Advances, 5, eaaw5406, https://doi.org/10.1126/sciadv.aaw5406, 2019.

Maier, N., Humphrey, N., Meierbachtol, T., and Harper, J.: Deformation motion tracks sliding changes through summer, western Greenland, Journal of Glaciology, 68, 187–196, https://doi.org/10.1017/jog.2021.87, 2022.

Marmota Engineering AG: Elephant shelter, monitoring of strain evolution in the concrete ring, Zoo Zurich, https://www.marmota.com/project_reference.php?pid=12, 2012.

Mellor, M. and Testa, R.: Effect of Temperature on the Creep of Ice, Journal of Glaciology, 8, 131–145, https://doi.org/10.3189/s0022143000020803, 1969.

Millstein, J. D., Minchew, B. M., and Pegler, S. S.: Ice viscosity is more sensitive to stress than commonly assumed, Communications Earth & Environment 2022 3:1, 3, 1–7, https://doi.org/10.1038/s43247-022-00385-x, 2022.

Niklès, M.: La diffusion Brillouin dans les fibres optiques : étude et application aux capteurs distribués, Ph.D. thesis, EPFL - Swiss Federal Technology Institute of Lausanne, Lausanne, 1997.

Nye, J. F.: The Mechanics of Glacier Flow, Journal of Glaciology, 2, 82–93, https://doi.org/10.3189/S0022143000033967, 1952.

Ohno, S., Iida, D., Toge, K., and Manabe, T.: Long-range measurement of Rayleigh scatter signature beyond laser coherence length based on coherent optical frequency domain reflectometry, Optics Express, 24, 19 651, https://doi.org/10.1364/OE.24.019651, 2016.

Patton, A. I., Rathburn, S. L., and Capps, D. M.: Landslide response to climate change in permafrost regions, Geomorphology, 340, 116–128, https://doi.org/10.1016/j.geomorph.2019.04.029, 2019.

https://doi.org/10.5194/egusphere-2026-3329
Preprint. Discussion started: 8 July 2026

Qi, C., Prior, D. J., Craw, L., Fan, S., Llorens, M.-G., Griera, A., Negrini, M., Bons, P. D., and Goldsby, D. L.: Crystallographic preferred orientations of ice deformed in direct-shear experiments at low temperatures, The Cryosphere, 13, 351–371, https://doi.org/10.5194/tc-13-351-2019, 2019.

Ranganathan, M. and Minchew, B.: A modified viscous flow law for natural glacier ice: Scaling from laboratories to ice sheets, Proceedings of the National Academy of Sciences of the United States of America, 121, e2309788121, https://doi.org/https://doi.org/10.1073/pnas.2309788121, 2024.

Roldán-Blasco, J.-P., Gilbert, A., Piard, L., Gimbert, F., Vincent, C., Gagliardini, O., Togaibekov, A., Walpersdorf, A., and Maier, N.: Creep enhancement and sliding in a temperate, hard-bedded alpine glacier, The Cryosphere, 19, 267–282, https://doi.org/10.5194/tc-19-267-2025, 2025.

Schenato, L.: A Review of Distributed Fibre Optic Sensors for Geo-Hydrological Applications, Applied Sciences, 7, 896, https://doi.org/10.3390/app7090896, 2017.

Schohn, C. M., Iverson, N. R., Zoet, L. K., Fowler, J. R., and Morgan-Witts, N.: Linear-viscous flow of temperate ice, Science, 387, 182–185, https://www.science.org/doi/10.1126/science.adp7708, 2025.

Schwerzmann, A., Funk, M., Blatter, H., Lüthi, M., Schwikowski, M., and Palmer, A.: A method to reconstruct past accumulation rates in alpine firn regions: A study on Fiescherhorn, Swiss Alps, Journal of Geophysical Research: Earth Surface, 111, https://doi.org/10.1029/2005JF000283, 2006.

Soller, B. J., Wolfe, M., and Froggatt, M. E.: Polarization resolved measurement of Rayleigh backscatter in fiber-optic components, in: Polarization Resolved Measurement of Rayleigh Backscatter in Fiber-optic Components, p. 3, Optical Society of America, Optical Society of America, Anaheim, 2005.

Soto, M. A., Bolognini, G., Di Pasquale, F., and Thévenaz, L.: Long-range Brillouin optical time-domain analysis sensor employing pulse coding techniques, Measurement Science and Technology, 21, 094024, https://doi.org/10.1088/0957-0233/21/9/094024, 2010.

Tateda, M., Horiguchi, T., Kurashima, T., and Ishihara, K.: First measurement of strain distribution along field-installed optical fibers using Brillouin spectroscopy, Journal of Lightwave Technology, 8, 1269–1272, https://doi.org/10.1109/50.59150, 1990.

Thévenaz, L.: Brillouin distributed time-domain sensing in optical fibers: state of the art and perspectives, Frontiers of Optoelectronics in China, 3, 13–21, https://doi.org/10.1007/s12200-009-0086-9, 2010.

Troilo, F., Gottardelli, S., Giordan, D., Dematteis, N., Godio, A., and Vincent, C.: Geophysical and geomatic recent surveys at Whymper hanging Glacier (Aosta Valley &#8211; Italy), https://doi.org/10.5194/egusphere-egu21-5178, 2021.

Troilo, F., Paolo, P., Gottardelli, S., Mondardini, L., Giordan, D., Dematteis, N., Piard, L., Gagliardini, O., Gilbert, A., and Vincent, C.: Basal thermal regime investigations at Whymper hanging Glacier (Aosta Valley &#8211; Italy), https://doi.org/10.5194/egusphere-egu22-7208, 2022.

Tyler, S., Holland, D., Zagorodnov, V., Stern, A., Sladek, C., Kobs, S., White, S., Suárez, F., and Bryenton, J.: Using distributed temperature sensors to monitor an Antarctic ice shelf and sub-ice-shelf cavity, Journal of Glaciology, 59, 583–591, https://doi.org/10.3189/2013JoG12J207, 2013.

Vincent, C., Thibert, E., Harter, M., Soruco, A., and Gilbert, A.: Volume and frequency of ice avalanches from Taconnaz hanging glacier, French Alps, Annals of Glaciology, 56, 17–25, https://doi.org/10.3189/2015AoG70A017, 2015.

Walter, F., Dreger, D. S., Clinton, J. F., Deichmann, N., and Funk, M.: Evidence for Near-Horizontal Tensile Faulting at the Base of Gornergletscher, a Swiss Alpine Glacier, Bulletin of the Seismological Society of America, 100, 458–472, https://doi.org/10.1785/0120090083, 2010.

Wilson, C. J. and Peternell, M.: Ice deformed in compression and simple shear: control of temperature and initial fabric, Journal of Glaciology, 58, 11–22, https://doi.org/10.3189/2012JoG11J065, 2012.

Youn, J. H., Song, K. Y., Martin-Lopez, S., Gonzalez-Herraez, M., and Fernández-Ruiz, M. R.: Brillouin expanded time-domain analysis based on dual optical frequency combs, Light: Science & Applications, 13, 149, https://doi.org/10.1038/s41377-024-01499-x, 2024.

Zoet, L. K. and Iverson, N. R.: A slip law for glaciers on deformable beds, Science, 368, https://doi.org/10.1126/science.aaz1183, 2020.